

1 **Revision 1**

2
3
4 **Dissolution-precipitation and self-assembly of serpentine nanoparticles**
5 **preceding chrysotile formation: Insights into the structure of proto-**
6 **serpentine**

7 ROMAIN LAFAY^{1,2*}, ALEJANDRO FERNANDEZ-MARTINEZ^{1,3}, GERMAN MONTES-
8 HERNANDEZ^{1,3}, ANNE LINE AUZENDE¹, AGNIESZKA POULAIN⁴

9
10 ¹ *Universite Grenoble Alpes, ISTERre, F-38041 Grenoble, France*

11 ² *Institute of Earth Sciences, University of Lausanne, CH-1015 Lausanne, Switzerland*

12 ³ *CNRS, ISTERre, F-38041 Grenoble, France*

13 ⁴ *ESRF, 71, Avenue des Martyrs, 38043 Grenoble, France*

14
15
16
17
18 * Corresponding authors: Romain Lafay (romain.lafay@unil.ch)

19
20
21
22
23
24
25
26
27
28
29
30
31
32
33
34
35
36
37
38
39
40
41
42
43

ABSTRACT

Any poorly crystalline serpentine-type mineral with a lack of recognizable textural or diffraction features for typical serpentine varieties (i.e. chryotile, lizardite, antigorite) is usually referred to as proto-serpentine. The formation of the so-called proto-serpentine seems ubiquitous in serpentinization reactions. It is related to dissolution-precipitation of strongly reactive particles prior to true serpentine formation (e.g. in veins where both chrysotile and proto-serpentine are described). However, the structural characteristics of proto-serpentine and its relation with serpentine crystalline varieties remain unclear. In this study a model describing the transformation from proto-serpentine to chrysotile is presented based on experimental chrysotile synthesis using thermogravimetric analyses, transmission electron microscopy and high-energy X-ray diffraction with pair distribution function analyses. The combination of the high resolution TEM and high-energy X-ray diffraction enables to resolve the local order of neo-formed particles and their structuration processes occurring during pure chrysotile formation (i.e. during the first three hours of reaction). The formation of individual nanotubes is preceded by the formation of small nanocrystals that already show a chrysotile short-range order, forming porous anastomosing features of hydrophilic crystallites mixed with brucite. This is followed by a hierarchical aggregation of particles into a fiber-like structure. These flake-like particles subsequently stack forming concentric layers with the chrysotile structure. Finally, the individualization of chrysotile nanotubes with a homogeneous distribution of diameter and lengths (several hundreds of nanometer in length) is observed. The competitive precipitation of brucite and transient serpentine during incipient serpentinization reaction indicates that both dissolution-precipitation and serpentine-particle aggregation processes operate to form individual chrysotile. This study sheds light into mineralization processes and sets a first milestone towards the identification of the factors controlling polymorph selection mechanisms in this fascinating system.

44 **Keywords:** proto-serpentine, pair distribution function, chrysotile, stacking, simulation

INTRODUCTION

45
46
47 Serpentine is a common mineral containing structural water with an ideal chemical
48 formula $Mg_3Si_2O_5(OH)_4$. The serpentine group of minerals contains different varieties, among
49 which the most commons forms are antigorite, consisting of periodic modulated layers,
50 (Kunze, 1956), lizardite, consisting of flat periodic layers, (Wicks and O'Hanley, 1988), and
51 chrysotile and polygonal serpentine, consisting in fibers, (Yada, 1967; Middleton and
52 Whittaker, 1976). Serpentes are mainly found in altered Earth oceanic lithosphere. Lizardite
53 and chrysotile are both involved it hydrothermal systems and are found in the same stability
54 domains (moderate temperature, bellow 400°C), whereas antigorite is the high-pressure/high
55 temperature serpentine variety (Evans et al., 1976; Evans, 2004; Wunder and Schreyer, 1997).
56 Chrysotile is one of the most common and studied cylindrical fibrous serpentine and consists
57 in the succession of tetrahedral sheets inserted between brucite-type magnesian octahedral
58 layers. The structural misfit between tetrahedral and octahedral sheets induces a concentric or
59 spiral curvature around the x or y axis (Whittaker, 1956b; Whittaker, 1956c; Whittaker,
60 1956a; Middleton and Whittaker, 1976) with a fivefold symmetry (Cressey and Whittaker,
61 1993; Cressey et al., 2010) and with the tetrahedral sheet inside (Pauling, 1930). Chrysotile is
62 considered as a thermodynamically metastable serpentine variety having a strong chemical
63 reactivity toward the formation of lizardite, even in the pure Mg system (Grauby et al., 1998;
64 Evans, 2004). The relationships between layered and tubular serpentine minerals, the overlap
65 between individual polymorphs and the frequent occurrence of turbostratism in serpentine
66 minerals (Trittschack et al., 2012) are of great interest in natural settings where both lizardite
67 and chrysotile coexist. Moreover, an advanced understanding of the atomic scale mineral
68 transformation mechanisms in the serpentine system remains necessary to understand mobile
69 elements or trace-metals cycle during oceanic lithosphere alteration.

70 While the structure of well-crystallized serpentine varieties has been determined from
71 X-ray and electron diffraction and transmission electron microscopy (TEM), proto-serpentine
72 is increasingly described as poorly crystalline serpentine precursor of undetermined fibrous
73 serpentines in experimental (Dufaud et al., 2009; Bloise et al., 2012; Godard et al., 2013;
74 Lafay et al., 2013) and natural (Andreani et al., 2008; Andreani et al., 2004; Plümper et al.,
75 2012) systems, especially in association with chrysotile. Chrysotile is generally present in
76 supersaturated systems and veins. In this context, the alteration of mantle-silicate minerals by
77 hydrothermal fluids is usually characterized by the development of cracks filled with
78 serpentine or by pseudomorphic polycrystalline serpentine features originated from
79 dissolution/precipitation processes (Wicks and Whittaker, 1977; Putnis, 2002). The
80 dissolution of mantle silicate (pyroxene and olivine) appears largely controlled by its
81 crystallographic orientation and fluid composition (Velbel, 1993; Velbel, 2009; Daval et al.,
82 2010; Daval et al., 2013) but, to our knowledge, the direct relation between dissolution
83 properties (e.g. rate, mechanisms) and secondary phase precipitation has never been explored.
84 However, the formation of serpentine mineral precursors to chrysotile, which subsequently
85 recrystallize into lizardite, is probably taking place in reaction rims at fluid-mineral interfaces
86 and is surely linked to surface reactivity.

87 During the last decades various experimental studies have attempted to reproduce
88 natural serpentinization features and to ascertain the main parameters controlling
89 serpentinization processes (Seyfried Jr and Dibble Jr, 1980; Macleod et al., 1994; James et al.,
90 2003; Seyfried Jr. et al., 2007; McCollom and Bach, 2009; Hövelmann et al., 2011). In this
91 way, serpentine phase's stability domains are continuously refined. Moreover, serpentine
92 synthesis methods, especially for chrysotile, have been developed since the mid of the last
93 century (Noll, 1950; Yada and Iishi, 1974; Yada and Iishi, 1977). Recent research has
94 attempted to develop more efficient synthesis protocols and to characterize the effect of

95 foreign elements on the mineral growth processes (Bloise et al., 2009; Korytkova and
96 Pivovarova, 2010; Korytkova et al., 2011; Lafay, Montes-Hernandez, et al., 2014). Some of
97 these studies have also aimed to get a better understanding of structural factors governing
98 natural chrysotile health hazards (Falini et al., 2006; Foresti et al., 2009; Turci et al., 2011).

99 The transformation from precursor phases (aqueous, colloidal or solid) to mineral
100 structures and the relation between mineral polymorphs is currently a very active research
101 area in the (bio)geosciences (De Yoreo et al., 2015). However, until now very few studies
102 have been devoted to the identification of the first steps of serpentine nucleation and growth at
103 laboratory scale, and many questions still remain unanswered concerning the transition from
104 the so-called proto-serpentine to crystalline serpentine. In a previous contribution we
105 highlighted that chrysotile synthesis at 300°C was characterized by the initial formation of a
106 poorly crystallized serpentine associated with brucite. Here we show that the competitive
107 precipitation of brucite and serpentine, progressively consumed via dissolution precipitation
108 processes, preceded the individualization and growth of single chrysotile nanotubes via a
109 progressive Ostwald ripening process (Lafay et al., 2013). The dissolution-precipitation
110 process was effective during the first 20 hours of reaction. The broad X-ray diffraction peaks
111 in the diffraction pattern of the serpentine precursor crystallites (first 2 hours of reaction) is
112 surely due to small coherent domain sizes, and also probably to turbostratic disorder along the
113 stacking direction, and to an amorphous component difficult to be interpreted from laboratory
114 X-ray data. In summary, dissolution re-precipitation processes could be systematically
115 involved in the transformation from proto-serpentine to the final crystalline varieties (Jancar
116 and Suvorov, 2006; Lafay et al., 2013).

117 In this study we expand on the efforts to decipher the nature of the amorphous and
118 nanocrystalline phases precursors that can be formed during the early steps of chrysotile
119 formation. For that purpose, this experimental study was based on an accurate sampling

120 period (half an hour) during the first steps of chrysotile synthesis (i.e. the first three hours). A
121 combination of thermogravimetric, TEM and high energy X-ray diffraction data, including
122 pair distribution function analyses, were performed in order to obtain new insights into the
123 structural characteristics of the serpentine precursor. Hereafter, an accurate model for
124 chrysotile structuration is proposed.

125 **MATERIALS AND METHODS**

126 Experimental synthesis

128 Semi-continuous chrysotile syntheses were conducted at 300°C and saturated pressure
129 (≈ 79 bar) respecting serpentine stoichiometry ($\text{Mg/Si} = 1.33$); starting with 300 ml of 1M
130 NaOH solution, 1.302 g of silica gel (H_2SiO_3) and 5.082 g of magnesium chloride
131 hexahydrate ($\text{MgCl}_2 \cdot 6\text{H}_2\text{O}$). The reactants were placed in a hastelloy C22 reactor (autoclave
132 with an internal volume of 0.6 L). The suspension was immediately stirred and heated using
133 constant mechanical agitation (300 rpm) and a heating jacket adapted to the reactor as early
134 described in Lafay et al. (2013). Six samples were collected from 10 ml dispersions sampled
135 approximately every half hour, between 40 minutes and three hours of reaction. After
136 centrifugation and fluid removal, the solid product was dried at 90 °C during 48 hours and
137 recovered for further thermogravimetric analyses (TGA), TEM and High-energy X-ray
138 diffraction measurements.

139 A synthetic brucite was produced by reacting 0.25 mol of chloride hexahydrate in 250
140 ml of 1M NaOH solution. Minerals consists in pure $\text{Mg}(\text{OH})_2$ hexagonal flakes with a size
141 ranging from few dozens of nanometers to few hundreds of nanometers and a width of about
142 20 nm.

143 Solid product characterization

144 Solid products were characterized by differential thermal analysis (DTA) and TGA
145 with a TGA/SDTA 851e Mettler Toledo instrument using about 10 mg of powder placed in a

146 platinum crucible of 150 μl with a pinhole. Analyses were performed using a heating rate of
147 $10\text{ }^{\circ}\text{C min}^{-1}$, and inert N_2 atmosphere of 50 ml min^{-1} . Sample mass loss and associated thermal
148 effects were obtained by TGA/DTA in a temperature range from $30\text{ }^{\circ}\text{C}$ to $1200\text{ }^{\circ}\text{C}$. The
149 instrumental theoretical T precision is $\pm 0.5\text{ }^{\circ}\text{C}$ and the weight sensitivity down to $0.1\text{ }\mu\text{g}$.
150 TGA apparatus was calibrated in terms of mass and temperature. Calcium oxalate was used
151 for the sample mass calibration. The melting points of three compounds (indium, aluminum
152 and copper) obtained from the DTA signals were used for the sample temperature calibration.
153 The TGA first derivative (so called differential thermogravimetry DTG) was used to better
154 identify mass loss steps and to determine the loss of mass associated with brucite and
155 serpentine phases (Viti, 2010; Lafay et al., 2013; Bloise et al., 2015).

156 Additionally, samples were loaded into kapton capillaries for high-energy synchrotron
157 X-ray diffraction measurements (HEXD). HEXD experiments allow recording a long
158 momentum transfer (Q) diffraction pattern, including good statistics for the diffuse scattering.
159 These patterns are usually called ‘total scattering patterns’. Total scattering experiments are
160 usually performed to study the local order of amorphous or poorly crystalline materials, where
161 the diffuse scattering accounts for a high proportion of the total X-ray scattering. HEXD
162 patterns of amorphous or disordered materials are usually analysed using the Pair Distribution
163 Function (PDF or $g(r)$) approach. In short, the PDF is the Fourier transform of the reduced
164 structure factor, $F(Q)$:

$$165 \quad F(Q) = Q[S(Q) - 1] \quad (\text{eq. 1})$$

$$166 \quad g(r) - 1 = \frac{1}{2\pi^2 r \rho} \int_0^{\infty} Q[S(Q) - 1] \sin(Qr) dr \quad (\text{eq. 2})$$

167 where r is the interatomic distance, ρ is the number density and $S(Q)$ is the structure factor.
168 The resulting PDF is a map of the interatomic distances in the sample. The PDF method
169 provides a different way to analyse short-range order, using a real space representation of the
170 scattering data. The PDF method has been use to describe the first stages of formation

171 inorganic materials and the structure of poorly crystalline minerals (Becker *et al.*, 2010;
172 Caraballo *et al.*, 2015; Fernandez-Martinez *et al.*, 2010; Gilbert *et al.*, 2004; Michel *et al.*,
173 2007). Given the high amount of diffuse scattering present in the diffraction pattern of
174 disordered minerals and of mineral precursors, the PDF provides a useful way to describe the
175 structural characteristics of these phases.

176 Total scattering patterns were acquired at beamline ID15B of the European
177 Synchrotron Radiation Facility (ESRF), Grenoble, France. Scattering data were collected with
178 a Perkin-Elmer flat-panel detector using the rapid-acquisition pair distribution function (PDF)
179 technique (Chupas *et al.*, 2003). Measurements of the samples and empty capillary were made
180 at ambient temperature in a range of Q from 0–25 \AA^{-1} . The X-ray wavelength ($\lambda = 0.14252 \text{\AA}$)
181 was refined using a NIST certified CeO_2 standard. Total scattering structure functions and
182 pair distribution functions were obtained using the PDFGetX3 software.

183 TEM was used to determine the shape and sizes of chrysotile nanotubes and of their
184 precursors. For that purpose, powders of samples were dispersed in ethanol and one drop of
185 the sample suspension was deposited on a holey carbon foil placed on conventional copper
186 micro-grids. TEM experiments were performed at the Institut de Minéralogie et de Physique
187 des Milieux et Cosmochimie (Paris, France) using a JEOL 2100F microscope operating at 200
188 kV, equipped with a field emission gun and a high-resolution pole piece achieving a point-to-
189 point resolution of 1.8 \AA , and at Cinam (Marseille, France) using a JEOL 3100 microscope
190 operating at 300 kV equipped with a LaB6 filament achieving a point-to-point resolution of
191 1.6 \AA .

192 Structural models for simulations

193 Models of minerals structures were used to simulate PDFs and interpret experimental
194 observations. For that purpose we created atomistic models of chrysotile nanotubes by rolling
195 lizardite layers along the [010] direction, and using average diameter dimensions obtained

196 from TEM images, of 7 and 14 nm for the radii of the inner and outer layers, respectively. The
197 curvature of the layers induces slight shortening and lengthening of Si-O and Mg-O inter-
198 atomic distances. However, maximum values of these distortions remain physically plausible
199 (see Electronic Annex). PDFs and diffraction patterns from these models were calculated
200 using routines from the Diffpy-CMI library (Juhás et al., 2015). Diffraction patterns were
201 calculated using the Debye equation formalism from non-periodic models of the structures
202 (Warren, 1969). Isotropic thermal displacement parameters for all atoms were set to $8 \cdot 10^{-3} \text{ \AA}^2$.
203 VESTA (Momma and Izumi, 2011) was used to represent the mineral structures used in this
204 study.

205
206
207
208

EXPERIMENTAL RESULTS

TGA, DTG, and DTA

209 TGA and DTG/DTA result are summarized in Figure 1, Tables 1 and 2. All TGA
210 curves are characterized by a continuous weight loss divided in different dehydroxylation
211 steps that show some variations from 1 to 3 hours of reaction. The total weight losses at 800
212 °C for all samples is about 29 % for the two first samples and 22-27 % for the four last
213 samples (Table 1). The weight loss below 200°C is attributed to release of molecular water;
214 this value remains higher than ~9 % (usually lower than 5 % for pure synthetic and natural
215 chrysotile (Falini et al., 2004; Viti, 2010; Lafay, Montes-Hernandez, et al., 2014)) suggesting
216 a high water retention by a porous material. The main weight loss occurs in the 200-800 °C
217 range showing a single or double stage, i.e., two distinct DTG maxima, (Table 2) that can be
218 linked to brucite and serpentine dehydroxylation. Before 1h30 min of reaction, DTG curves
219 are characterized by a peak at a temperature comprised between 250 and 400 °C related to the
220 decomposition of brucite particles (Blaauw et al., 1979; Wang et al., 1998). Dehydroxylation
221 peak for brucite completely disappears after 2 hours of reaction. Note that in previous
222 experiments brucite was clearly observed up to 4 hours of reaction (Lafay et al., 2013).

223 However we found relicts of brucite after 3 hours of reaction (see TEM measurements
224 section). The time-discrepancy for brucite disappearance could be due to the use of different
225 reactors, implying different vessel material and different volume. After 1h30 min a clear
226 dehydroxylation event appears at 537 °C (Fig. 1c) linked to a weak endothermic peak at 541
227 °C (Table 1). The development of a strong endothermic peak between 2 hours and 2h50 min
228 of reaction corresponds to the decomposition of particles from the serpentine group (Cattaneo
229 et al., 2003). Here, the weight loss relative to serpentine destabilization (400-700 °C) for the
230 two lasts samples remain in the 11.5-14 % range and is consistent with theoretical water
231 content for serpentine minerals. The DTG peak splits after 2h25 of reaction (one component
232 centred at 535°C and one at 460 °C, Table 2, Fig. 1e) underlying the presence of two kinds of
233 particles or representing the breakdown stage of distinct inner and outer OH groups (Franco et
234 al., 2006). Additionally, the endothermic DTA peak shifts to higher temperature (553°C, Fig.
235 1d). After 2h50 min of reaction the DTG doublet remains present and linked to DTA
236 endothermic doublet. However the main weight loss component centred at ca. 554°C (Fig. 1f)
237 supports the presence of a dominant serpentine component.

238 Since the beginning of the reaction (i.e. after only 40 minutes of reaction) an
239 exothermic peak is observed in the DTA curves in the 670-715°C range with an onset
240 oscillating between 640°C and 660°C (except after 1 hour, peak at 634 °C). The peak position
241 does not match with the typical temperature of ca. 820 °C sharp exothermic peak related to
242 the crystallization of the remaining amorphous anhydrous meta-chrysotile ($Mg_3Si_2O_7$) into
243 forsterite (Mg_2SiO_4) (Viti, 2010). However, we relate this peak to the process of end of
244 dehydration and massive crystallization of forsterite and enstatite. The shift of exothermic
245 DTA peak toward lower temperature referring to pure serpentine in longer experiments (Table
246 1) might be due to a combination of the difference in shape, size and density of particles

247 obtained during the first steps of the chrysotile synthesis (Chatzistavrou et al., 2006;
248 Trittschack et al., 2013).

249 In addition to the reaction pathway described in (Lafay et al., 2013), a more detailed
250 description of the fluctuation observed in the DTA and TGA/DTG curves is given here for the
251 early stages of chrysotile synthesis. We confirmed the presence of brucite in the early stage of
252 the reaction. The oscillating DTG/DTA signal ranging from 200 °C to 800 °C is linked to a
253 continuous evolution of the abundance, and physical properties of brucite and serpentine-type
254 particles attesting for a non-apparent-equilibrium of the system until three hours of reaction.

255 TEM

256 TEM investigations reveals major changes of particles sizes and morphologies during
257 the first stages of serpentine synthesis until the formation of chrysotile with a typical average
258 width ranging between 16 and 20 nm and a variable length from 100 nm to 800 nm. The
259 tunnel width remains extremely monodisperse after 3 hours of reaction and is about 7.5-8 nm.

260 During the first hour of reaction we note the presence of brucite associated with a
261 matrix of flake-like particles constituting an anastomosing network (Fig. 2a and b). The
262 presence of brucite in the early steps of the synthesis is consistent with TGA/DTG
263 measurements and previous work (Lafay et al., 2013). The sensitivity of this medium to
264 electron beam made it difficult to perform TEM characterization with high magnification.
265 After 40 minutes, the medium is already pre-structured, as shown by the dense regions and the
266 diffraction pattern in Figure 2a which is characterized by few diffraction bands rather than a
267 diffuse illumination signal. However no sharp diffraction spots specific for a satisfying crystal
268 structure were observed. A few tubular fibers (or conical) can be observed, yet their
269 occurrence remains rare. In addition, between 40 minutes (corresponding to the end of the
270 heating) and 1 hour of reaction, the anastomosed features are replaced by a porous medium
271 with large fiber-like morphologies as a result of particle aggregation (see Figure 2b). These

272 fiber-like aggregates display wide (up to 100 nm) and variable diameters and are poorly
273 structured with respect to typical synthetic chrysotile (maximum ~20 nm diameter). In this
274 highly energetic system, heterogeneous particles probably tend to reach a greater structuration
275 and homogenization to lower the misfit energy. The number of manifested individual tubes
276 increase with respect to experiment after 40 minutes.

277 After 1h30 of reaction the presence of individual particles is clearly visible and two
278 kinds of crystallites can be distinguished; small flakes co-existing with individual nanotubes,
279 characterized by various sizes and morphology (Fig. 2c). Only few tubes have the typical
280 width and length of the chrysotile reference (which is taken at the end of the reaction). Most
281 of them are smaller than 100 nm in length and they exhibit beveled edges and ovoid shapes
282 like nanorods.

283 Between 2 hours and 2h25 min of reaction individual chrysotile with characteristic
284 widths lower than 20 nm are observed (Fig. 3a). The apparent different width of nanotubes
285 walls might correspond to a difference in phyllosilicate sheets layers and/or atomic density.
286 After 2h50 min of reaction well crystalized individual nanotubes with thin walls become the
287 dominant species (Fig. 3b). This chrysotile type corresponds to the typical end-member
288 minerals observed after long synthesis experiments (Lafay et al., 2013). As mentioned before,
289 the apparent absence of brucite regarding the TGA signal is due to the presence of only rare
290 relicts of brucite (Fig. 3b). At this point, the chrysotile morphology can be considered as an
291 equilibrium morphology that lowers the energy due to the mismatch between octahedral and
292 tetrahedral sheets of serpentine in the MgO-SiO₂-H₂O system (pure Mg system). The
293 occurrence of a double DTG/DTA signal after 2h25 min of reaction is consistent with TEM
294 observations underlying the presence of two kinds of chrysotile particles around 2h of
295 reaction.

296

297 High energy X-ray diffraction and Pair Distribution Function analysis

298 Structure factors, $S(Q)$, obtained from high-energy X-ray diffraction experiments and
299 the corresponding PDFs of the synthetic samples and synthetic brucite are presented in Figure
300 4. The most striking characteristic is the fact that, from the beginning of the experiment, all
301 the $S(Q)$ and PDFs show similar features. As expected from TGA and TEM characterization,
302 brucite is present in the samples taken before 1h30 min, and its diffraction peaks can be
303 distinguished in the form of a shoulder in the diffraction peak at $\sim 2.45 \text{ \AA}^{-1}$. After 1h30 min of
304 reaction all the $S(Q)$ and PDFs reveal features common to that of the chrysotile end-member.

305 An interesting evolution of the low Q peaks is observed (see Figure 4b). The (004)
306 diffraction peak, at 1.7 \AA^{-1} , is only observed after 1h30 min. Note that this notation
307 corresponds to the lizardite planar structure (Mellini, 1982; Auzende et al., 2006), which has
308 been used to create chrysotile atomistic models; the c axis corresponds to the stacking along
309 the radial direction of the nanotubes. Analysis of the PDFs (Fig. 4c) gives information about
310 the evolution of the coherent domain size, and, again, about the presence of brucite. The
311 decaying intensity of the inter-atomic correlations at long distances is due to a coherent
312 domain size effect, which changes slightly from $\sim 27 \text{ \AA}$ at 40 min up to 32 \AA for the chrysotile
313 obtained after 2h50 min. The relatively small increase in the coherent domain size for
314 experimental product is probably due to the existence of defects formed during minerals
315 structuration.

316 The structuration of chrysotile particles is accompanied by an increase of the Si-O and
317 Si-Si bond intensity in the PDFs (Fig. 4d). We used synthetic brucite and synthetic chryotile
318 obtained after 3 hours of reaction as endmembers to fit all the intermediate PDFs. Note here
319 that the PDFs for chrysotile after 2h50 min and 30h of reactions (Lafay et al., 2013) are
320 identical. All patterns can be fitted using a linear combination between this two end members
321 (see Fig. 5). Here the brucite component is not significant and is no longer required after 1 h

322 30 min of reaction. This result indicates that the chrysotile local order is already present in the
323 samples at early stages of crystallization and that, after 1h30 min of reaction, the chrysotile
324 end-member PDF is enough to fit experimental PDFs results.

325 Additionally, simulations of the evolution of the low-Q part of experimental S(Q)
326 curves (Fig. 4a and b) have been performed by creating chrysotile nanotube structures formed
327 by one, two or four concentric walls (Fig. 6). The simulations reveal that the peak at $\sim 1.7 \text{ \AA}^{-1}$,
328 corresponding to the (004) reflection in lizardite, increases proportionally to the number of
329 concentric stacked layers. The structure factor of experimental products after 40 minutes of
330 reaction display no features characteristic for multi-wall nanotubes. After 1h and 1h30
331 minutes the experimental S(Q) match with a model of two concentric wall layers. Between
332 1h30 min and 2h of reaction the serpentine products acquire the characteristic features for a
333 coherent concentric stacking of at least four serpentine-sheets. The structure factor does not
334 change anymore after 2h of reaction. Note that the only way to reproduce the peak intensity is
335 the stacking of concentric curved lizardite sheets. Tests using physical mixing of single-
336 walled particles with different diameters never reproduced the low Q level of intensity
337 observed for well crystallized chrysotile.

338 **DISCUSSION AND IMPLICATIONS**

339 Serpentinization of ultramafic rocks is a widespread hydration reaction that take
340 place from subsurface lithospheric environment to deep subduction zones and considerably
341 affects rheological and chemical properties of peridotite rocks. It is know that fluid circulation
342 in natural environments contributes to large scale mass transfer and Mg/Si ratio changes
343 during serpentinization (Niu, 2004; Boschi et al., 2006). Pristine mineral alteration involves
344 a dramatic decrease of rock density and rock strength (Escartin et al., 2001). Moreover, rock
345 hydration processes induce small-scale chemical redistributions and important element
346 entrapment (e.g. B, Li, Cl, As, Sb) likely to be released or exchanged during serpentine phase

347 transformation-recrystallization (Vils et al., 2011) and serpentine dehydration in convergent
348 zones (Deschamps et al., 2013). Some aqueous species greatly increase serpentinization rate
349 in hydrothermal systems and various physicochemical parameters may affect serpentine
350 mineralogical properties (Korytkova et al., 2011; Andreani et al., 2013; Lafay, Janots, et al.,
351 2014). Prior to serpentine formation, proto-serpentine has already been described as an
352 amorphous material or 'matrix' in natural samples (Plümper et al., 2014). In most studies,
353 proto-serpentine is designated as a poorly crystallized and poorly organized serpentine
354 aggregate from which other serpentine varieties start to growth (Andreani et al., 2008), with a
355 fibrous microstructure (Dufaud et al., 2009; Ryu et al., 2011).

356 The structural transformation at atomic scale, from serpentine precursor to serpentine
357 endmembers, in the MgO-SiO₂-H₂O system account for small scale mass transfer at mineral
358 scale during olivine and pyroxene alteration. The study of chrysotile structuration from free-
359 fluid in experimental system - which can be linked to serpentine veins in natural systems
360 (Andreani et al., 2004) - enables the exploration of the progressive serpentine physical
361 properties changes and might account for small scale chemistry changes and mobile element
362 migration in serpentine veins (Benton et al., 2004).

363 Structuration model from serpentine precursor to chrysotile formation

364 The results from these analyses dismiss the hypothesis of a totally amorphous
365 material. In many studies, chrysotile is considered as a metastable varieties characterizing the
366 first steps of serpentine crystallization, and later re-crystallizing into polygonal serpentine and
367 lizardite (Grauby et al., 1998). In this study, we have focused only on the first part of this
368 process, with chrysotile being the final end-member of the reaction, considered as a reference.

369 As already shown in Lafay et al., (2013), we confirmed that the formation of
370 homogeneous chrysotile is preceded by a stage where transitory phases are rapidly consumed
371 and transformed at least partly by dissolution-precipitation processes to supply chrysotile

372 growth. Such assumption is supported by (1) the precipitation of transient brucite and
373 serpentine that remains distinguishable by TGA and TEM analyses up to 2 hours of reaction,
374 (2) a progressive evolution of mineral phase properties and proportion accompanied by a loss
375 of total water visible by DTG/DTA pattern in the brucite-serpentine dehydroxylation range
376 from 40 minutes to 2 h of reaction, (3) the change in particle size from wide to thin fiber-like
377 particles.

378 An interesting feature from the DTG/DTA data is the important loss of mass related to
379 serpentine minerals before 1 hour of reaction, this despite the absence of the typical
380 dehydroxylation peak. This confirm the presence of small heterogeneous flack-type particles
381 not distinguishable by conventional X-ray powder diffraction analyses. However, the short-
382 range structure of chrysotile is already recognizable by PDF analyses after a short reaction
383 time (Figs 4 and 5). We reinforce the idea that TGA features are extremely sensitive to the
384 presence of dissolution-precipitation processes and the ensuing changes occurring in the
385 intermediate stage of reaction with the formation of transitory phases. The intensity of the
386 dehydroxylation peak appears to be dependent of the stacking properties and the formation of
387 long-range order in the chrysotile precursors. This could translate into a distribution of
388 dehydroxylation temperatures leading to the formation of several peaks (Fig. 1e) instead of the
389 single peak generally observed for crystalline chrysotile (Viti, 2010; Lafay et al., 2013; Bloise
390 et al., 2015)

391 High-energy X-ray diffraction measurements (including PDF analyses) coupled with
392 XRD modelling and TEM characterization enables to depict the specific case of chrysotile
393 formation. The different experimental observations converge towards a picture where
394 particles exhibiting chrysotile short-range order are already formed during the first stages of
395 reaction and co-exist with brucite (Figs. 2, 4 and 5) and probably other serpentine-type
396 particles (few tiny nanotubes are already present during the incipient reaction). TEM

397 observations after 1 hour of reaction show how these particles aggregate forming elongated
398 wide fiber-like shapes. Interestingly, the size of these aggregates is larger than the typical
399 diameters of the final chrysotile tubes (see Figure 2b). This could be an indicator for the
400 formation of an intermediate meso-structure that is later affected by dissolution-
401 (re)precipitation and structuration processes. The nanoscopic character of these nano-
402 crystalline flake-like particles suggests that they contain a large proportion of edge sites, with
403 -OH groups of variable reactivity.

404 For a reaction times greater than 1h30 min, an increase of the intensity of the
405 diffraction peak along the stacking direction is observed, which can be explained by an
406 increase in stacking of serpentine sheets and the structuration of chrysotile with a multi-wall
407 structure (Fig. 6). This coincides with the observation of individual nanorods and the first
408 visible structured nanotubes. We estimate that before 1h of reaction, the possible existence of
409 structured nanotubes (*i.e.*, coherent concentric serpentine sheets) remains too small to be
410 distinguishable by high-energy X-ray diffraction measurements. Obviously, after 1h30 min
411 the system remains heterogeneous, but previously observed poorly structured nano-fibers tend
412 to be replaced by short nanotubes (nanorods) and individual nanotubes (Fig. 2c). This
413 observation is consistent with the appearance of the typical serpentine dehydroxylation peak
414 in the DTG/DTA pattern. In the final stage, a continuous structuration through stacking of
415 coherent serpentine-sheets (Fig. 5) and the formation of longer tubes (Figure 3) is observed
416 with only minor changes in the diffraction patterns.

417 In addition to the dissolution-precipitation processes previously discussed, we
418 postulate that the kinetic sequence goes from a disordered pre-structured gel phase with
419 numerous nucleation centers (Fig. 1a) that evolves through time, to a high energy fiber-like
420 morphologies with various diameters and forms (tubular, flakes-like and conical). We propose
421 that the tubular geometry observed with monodisperse diameter can be considered as the

422 equilibrium morphology for the present conditions and chemical system. Several clues
423 suggest that transformation observed here are in adequation with later chrysotile to lizardite
424 transition proposed from previous experimental studies (Grauby et al., 1998) and
425 mineralization occurring in natural systems.

426 Our identification of pre-formed short-range ordered particles also support a
427 mechanism of self-assembly or aggregation-based growth (Fig. 7) to minimize energy. This
428 mechanism of particle-attachment has now been identified in various synthetic, biogenic, and
429 geologic environments (De Yoreo *et al.*, 2015). Aggregation and oriented attachment of pre-
430 formed nanoparticles have been reported to be active mechanisms of other common mineral
431 formation such like goethite (Banfield *et al.*, 2000; Guyodo *et al.*, 2003), ferrihydrite (Li *et*
432 *al.*, 2012) magnetite (Baumgartner *et al.*, 2013) or gypsum (Stawski *et al.*, 2016; Van
433 Driessche *et al.*, 2012), to name the most representative ones. This mechanism is comparable
434 to the one proposed for the structuration of imogolite (Levard et al., 2010), another tubular
435 mineral variety. However, while geological contexts are varied, few studies have addressed
436 hydrothermal conditions due to the difficulty associated with their study. Here, we show an
437 ex-situ study of hydrothermal growth of serpentine from a proto-serpentine precursor.

438 At an advanced stage of crystallization, after brucite consumption, the presence of
439 Ostwald ripening processes cannot be neglected. The present results provide a way to address
440 the role of this aggregation process in the incipient formation of serpentine in natural systems.
441 The differentiation towards other serpentine varieties remains to be explored. For that
442 purpose, further investigations under different physicochemical parameters (e.g. temperature,
443 pressure, impurities, CO₂/H₂O activity) are on-going to ascertain the mechanisms of
444 formation of other serpentine varieties such as lizardite and antigorite. It should be noted that
445 the proficiency to understand the structuration mechanism of nanomaterials remains of great

446 interest for example in applied physics for single- or multi-wall carbon nanotube synthesis
447 (Martel et al., 1998).

448

Acknowledgments

449 This work was supported by the French National Center for Scientific Research (CNRS) and
450 the University Joseph Fourier (UJF) in Grenoble for financial support. The authors are
451 grateful to R. Chiriac and F. Toche for TGA analyses. We thank the ESRF for the allocation
452 of beamtime. Funding from the AGIR programme of the University Grenoble Alpes is
453 acknowledged. R. Lafay thanks L.P. Baumgartner for granting me the time to achieve this
454 study in Lausanne.

455

References cited

- 456
457
458 Andreani, M., Baronnet, A., Boullier, A.-M. & Gratier, J.-P. (2004). A microstructural study of a “crack-seal”
459 type serpentine vein using SEM and TEM techniques. *European Journal of Mineralogy* **16**, 585–595.
- 460 Andreani, M., Daniel, I. & Pollet-Villard, M. (2013). Aluminum speeds up the hydrothermal alteration of
461 olivine. *American Mineralogist* **98**, 1738–1744.
- 462 Andreani, M., Grauby, O., Baronnet, A. & Muñoz, M. (2008). Occurrence, composition and growth of
463 polyhedral serpentine. *European Journal of Mineralogy* **20**, 159–171.
- 464 Auzende, A.-L., Pellenq, R. J.-M., Devouard, B., Baronnet, A. & Grauby, O. (2006). Atomistic calculations of
465 structural and elastic properties of serpentine minerals: the case of lizardite. *Physics and Chemistry of*
466 *Minerals* **33**, 266–275.
- 467 Banfield, J. F., Welch, S. A., Zhang, H., Ebert, T. T. & Penn, R. L. (2000). Aggregation-based crystal growth
468 and microstructure development in natural iron oxyhydroxide biomineralization products. *Science* **289**,
469 751–754.
- 470 Baumgartner, J., Dey, A., Bomans, P. H., Le Coadou, C., Fratzl, P., Sommerdijk, N. A. & Faivre, D. (2013).
471 Nucleation and growth of magnetite from solution. *Nature materials* **12**, 310–314.
- 472 Becker, J., Bremholm, M., Tyrsted, C., Pauw, B., Jensen, K. M. O., Eltzholt, J., Christensen, M. & Iversen, B. B.
473 (2010). Experimental setup for in situ X-ray SAXS/WAXS/PDF studies of the formation and growth of
474 nanoparticles in near-and supercritical fluids. *Journal of Applied Crystallography*. International Union
475 of Crystallography **43**, 729–736.
- 476 Benton, L. D., Ryan, J. G. & Savov, I. P. (2004). Lithium abundance and isotope systematics of forearc
477 serpentinites, Conical Seamount, Mariana forearc: Insights into the mechanics of slab-mantle exchange
478 during subduction. *Geochemistry, Geophysics, Geosystems* **5**.
- 479 Blaauw, C., Stroink, G., Leiper, W. & Zentilli, M. (1979). Crystal-field properties of Fe in brucite Mg(OH)₂.
480 *physica status solidi (b)* **92**, 639–643.
- 481 Bloise, A., Belluso, E., Barrese, E., Miriello, D. & Apollaro, C. (2009). Synthesis of Fe-doped chrysotile and
482 characterization of the resulting chrysotile fibers. *Crystal Research and Technology* **44**, 590–596.
- 483 Bloise, A., Belluso, E., Catalano, M., Barrese, E., Miriello, D. & Apollaro, C. (2012). Hydrothermal Alteration
484 of Glass to Chrysotile. *Journal of the American Ceramic Society* **95**, 3050–3055.
- 485 Bloise, A., Catalano, M., Barrese, E., Gualtieri, A. F., Gandolfi, N. B., Capella, S. & Belluso, E. (2015).
486 TG/DSC study of the thermal behaviour of hazardous mineral fibres. *Journal of Thermal Analysis and*
487 *Calorimetry* 1–15.
- 488 Boschi, C., Früh-Green, G. L., Delacour, A., Karson, J. A. & Kelley, D. S. (2006). Mass transfer and fluid flow
489 during detachment faulting and development of an oceanic core complex, Atlantis Massif (MAR 30 N).
490 *Geochemistry, Geophysics, Geosystems* **7**.
- 491 Caraballo, M. A., Michel, F. M. & Hochella, M. F. (2015). The rapid expansion of environmental mineralogy in
492 unconventional ways: Beyond the accepted definition of a mineral, the latest technology, and using
493 nature as our guide. *American Mineralogist*. MINERALOGICAL SOC AMER, 3635 CONCORDE
494 PKWY STE 500, CHANTILLY, VA 20151-1125 USA **100**, 14–25.
- 495 Cattaneo, A., Gualtieri, F. & Artioli, G. (2003). Kinetic study of the dehydroxylation of chrysotile asbestos with
496 temperature by in situ XRPD. *Physics and Chemistry of Minerals* **30**, 177–183.

- 497 Chatzistavrou, X., Zorba, T., Chrissafis, K., Kaimakamis, G., Kontonasaki, E., Koidis, P. & Paraskevopoulos, K.
498 M. (2006). Influence of particle size on the crystallization process and the bioactive behavior of a
499 bioactive glass system. *Journal of Thermal Analysis and Calorimetry* **85**, 253–259.
- 500 Chupas, P. J., Qiu, X., Hanson, J. C., Lee, P. L., Grey, C. P. & Billinge, S. J. (2003). Rapid-acquisition pair
501 distribution function (RA-PDF) analysis. *Journal of Applied Crystallography* **36**, 1342–1347.
- 502 Cressey, B. A. & Whittaker, E. J. W. (1993). Five-Fold Symmetry in Chrysotile Asbestos Revealed by
503 Transmission Electron Microscopy. *Mineralogical Magazine* **57**, 729–732.
- 504 Cressey, G., Cressey, B. A., Wicks, F. J. & Yada, K. (2010). A disc with fivefold symmetry: the proposed
505 fundamental seed structure for the formation of chrysotile asbestos fibres, polygonal serpentine fibres
506 and polyhedral lizardite spheres. *Mineralogical Magazine* **74**, 29–37.
- 507 Daval, D., Hellmann, R., Corvisier, J., Tisserand, D., Martinez, I. & Guyot, F. (2010). Dissolution kinetics of
508 diopside as a function of solution saturation state: macroscopic measurements and implications for
509 modeling of geological storage of CO₂. *Geochimica et Cosmochimica Acta* **74**, 2615–2633.
- 510 Daval, D., Hellmann, R., Saldi, G. D., Wirth, R. & Knauss, K. G. (2013). Linking nm-scale measurements of the
511 anisotropy of silicate surface reactivity to macroscopic dissolution rate laws: New insights based on
512 diopside. *Geochimica et Cosmochimica Acta* **107**, 121–134.
- 513 De Yoreo, J. J. *et al.* (2015). Crystallization by particle attachment in synthetic, biogenic, and geologic
514 environments. *Science*. American Association for the Advancement of Science **349**, 6760.
- 515 Deschamps, F., Godard, M., Guillot, S. & Hattori, K. (2013). Geochemistry of subduction zone serpentinites: A
516 review. *Lithos* **178**, 96–127.
- 517 Dufaud, F., Martinez, I. & Shilobreeva, S. (2009). Experimental study of Mg-rich silicates carbonation at 400
518 and 500 C and 1 kbar. *Chemical Geology* **265**, 79–87.
- 519 Escartin, J., Hirth, G. & Evans, B. (2001). Strength of slightly serpentinized peridotites: Implications for the
520 tectonics of oceanic lithosphere. *Geology* **29**, 1023–1026.
- 521 Evans, B. (2004). The serpentinite multisystem revisited: Chrysotile is metastable. *international Geology*
522 *review* **46**, 479–506.
- 523 Evans, B. W., Johannes, W., Oterdoom, H. & Trommsdorff, V. (1976). Stability of chrysotile and antigorite in
524 the serpentinite multisystem. *Schweizerische Mineralogische und Petrographische Mitteilungen* **56**, 79–
525 93.
- 526 Falini, G., Foresti, E., Gazzano, M., Gualtieri, A. F., Leoni, M., Lesci, I. G. & Roveri, N. (2004). Tubular-
527 Shaped Stoichiometric Chrysotile Nanocrystals. *Chemistry – A European Journal* **10**, 3043–3049.
- 528 Falini, G., Foresti, E., Lesci, I. G., Lunelli, B., Sabatino, P. & Roveri, N. (2006). Interaction of Bovine Serum
529 Albumin with Chrysotile: Spectroscopic and Morphological Studies. *Chemistry – A European Journal*
530 **12**, 1968–1974.
- 531 Fernandez-Martinez, A., Timon, V., Román-Ross, G., Cuello, G. J., Daniels, J. E. & Ayora, C. (2010). The
532 structure of schwertmannite, a nanocrystalline iron oxyhydroxysulfate. *American Mineralogist* **95**,
533 1312–1322.
- 534 Foresti, E., Fornero, E., Lesci, I. G., Rinaudo, C., Zuccheri, T. & Roveri, N. (2009). Asbestos health hazard: A
535 spectroscopic study of synthetic geoinspired Fe-doped chrysotile. *Journal of Hazardous Materials* **167**,
536 1070–1079.

- 537 Franco, F., Pérez-Maqueda, L. A., Ramírez-Valle, V. & PÉREZ-RODRÍGUEZ, J. L. (2006). Spectroscopic
538 study of the dehydroxylation process of a sonicated antigorite. *European journal of mineralogy* **18**,
539 257–264.
- 540 Gilbert, B., Huang, F., Zhang, H., Waychunas, G. A. & Banfield, J. F. (2004). Nanoparticles: strained and stiff.
541 *Science (New York, N.Y.)* **305**, 651–654.
- 542 Godard, M., Luquot, L., Andreani, M. & Gouze, P. (2013). Incipient hydration of mantle lithosphere at ridges: A
543 reactive-percolation experiment. *Earth and Planetary Science Letters* **371**, 92–102.
- 544 Grauby, O., Baronnet, A., Devouard, B., Schoumacker, K. & Demirdjian, L. (1998). The chrysotile-polygonal
545 serpentine-lizardite suite synthesized from a 3MgO-2SiO₂-excess H₂O gel. paper presented at the The
546 7th International Symposium on Experimental Mineralogy, Petrology, and Geochemistry, Orléans,
547 Abstracts. Terra Nova, supplement, 24.
- 548 Guyodo, Y., Mostrom, A., Lee Penn, R. & Banerjee, S. K. (2003). From Nanodots to Nanorods: Oriented
549 aggregation and magnetic evolution of nanocrystalline goethite. *Geophysical Research Letters* **30**,
550 1512.
- 551 Hövelmann, J., Austrheim, H., Beinlich, A. & Anne Munz, I. (2011). Experimental study of the carbonation of
552 partially serpentinized and weathered peridotites. *Geochimica et Cosmochimica Acta* **75**, 6760–6779.
- 553 James, R. H., Allen, D. E. & Seyfried, W. (2003). An experimental study of alteration of oceanic crust and
554 terrigenous sediments at moderate temperatures (51 to 350 C): Insights as to chemical processes in
555 near-shore ridge-flank hydrothermal systems. *Geochimica et Cosmochimica Acta* **67**, 681–691.
- 556 Jancar, B. & Suvorov, D. (2006). The influence of hydrothermal-reaction parameters on the formation of
557 chrysotile nanotubes. *Nanotechnology* **17**, 25–29.
- 558 Juhás, P., Farrow, C. L., Yang, X., Knox, K. R. & Billinge, S. J. L. (2015). Complex modeling: a strategy and
559 software program for combining multiple information sources to solve ill posed structure and
560 nanostructure inverse problems. *Acta crystallographica. Section A, Foundations and advances*.
561 International Union of Crystallography **71**, 562–8.
- 562 Korytkova, E., Brovkin, A., Maslennikova, T., Pivovarova, L. & Drozdova, I. (2011). Influence of the
563 physicochemical parameters of synthesis on the growth of nanotubes of the Mg₃Si₂O₅(OH)₄
564 composition under hydrothermal conditions. *Glass Physics and Chemistry* **37**, 161–171.
- 565 Korytkova, E. & Pivovarova, L. (2010). Hydrothermal synthesis of nanotubes based on
566 (Mg,Fe,Co,Ni)₃Si₂O₅(OH)₄ hydrosilicates. *Glass Physics and Chemistry* **36**, 53–60.
- 567 Kunze, G. (1956). Die gewellte Struktur des Antigorits, I. *Zeitschrift für Kristallographie - Crystalline Materials*
568 **108**, 82–107.
- 569 Lafay, R., Janots, E. & Montes-Hernandez, G. (2014a). Lithium control on experimental serpentinization
570 processes: implications for natural systems. .
- 571 Lafay, R., Montes-Hernandez, G., Janots, E., Auzende, A.-L., Chiriac, R., Lemarchand, D. & Toche, F. (2014b).
572 Influence of trace elements on the textural properties of synthetic chrysotile: Complementary insights
573 from macroscopic and nanoscopic measurements. *Microporous and Mesoporous Materials* **183**, 81–90.
- 574 Lafay, R., Montes-Hernandez, G., Janots, E., Chiriac, R., Findling, N. & Toche, F. (2013). Nucleation and
575 Growth of Chrysotile Nanotubes in H₂SiO₃/MgCl₂/NaOH Medium at 90 to 300° C. *Chemistry-A*
576 *European Journal* **19**, 5417–5424.
- 577 Levard, C. *et al.* (2010). Formation and growth mechanisms of imogolite-like aluminogermanate nanotubes.
578 *Chemistry of materials* **22**, 2466–2473.

- 579 Li, D., Nielsen, M. H., Lee, J. R., Frandsen, C., Banfield, J. F. & De Yoreo, J. J. (2012). Direction-specific
580 interactions control crystal growth by oriented attachment. *Science* **336**, 1014–1018.
- 581 Macleod, G., McKeown, C., Hall, A. J. & Russell, M. J. (1994). Hydrothermal and oceanic pH conditions of
582 possible relevance to the origin of life. *Origins of Life and Evolution of the Biosphere* **24**, 19–41.
- 583 Martel, R., Schmidt, T., Shea, H., Hertel, T. & Avouris, P. (1998). Single- and multi-wall carbon nanotube field-
584 effect transistors. *Applied Physics Letters* **73**, 2447–2449.
- 585 McCollom, T. M. & Bach, W. (2009). Thermodynamic constraints on hydrogen generation during
586 serpentinization of ultramafic rocks. *Geochimica et Cosmochimica Acta* **73**, 856–875.
- 587 Mellini, M. (1982). The crystal structure of lizardite 1T; hydrogen bonds and polytypism. *American*
588 *Mineralogist* **67**, 587–598.
- 589 Michel, F. M. *et al.* (2007). The structure of ferrihydrite, a nanocrystalline material. *Science* **316**, 1726–1729.
- 590 Middleton, A. P. & Whittaker, E. (1976). The structure of povlen-type chrysotile. *Canadian Mineralogist* **14**,
591 301–306.
- 592 Momma, K. & Izumi, F. (2011). VESTA 3 for three-dimensional visualization of crystal, volumetric and
593 morphology data. *Journal of Applied Crystallography*. International Union of Crystallography **44**,
594 1272–1276.
- 595 Niu, Y. (2004). Bulk-rock major and trace element compositions of abyssal peridotites: implications for mantle
596 melting, melt extraction and post-melting processes beneath mid-ocean ridges. *Journal of Petrology* **45**,
597 2423–2458.
- 598 Noll, von W. (1950). Synthesen im System MgO/SiO₂/H₂O. *Zeitschrift für anorganische Chemie* **261**, 1–25.
- 599 Pauling, L. (1930). The structure of the chlorites. *Proceedings of the National Academy of Sciences of the United*
600 *States of America* **16**, 578.
- 601 Plümper, O., Beinlich, A., Bach, W., Janots, E. & Austrheim, H. (2014). Garnets within geode-like serpentinite
602 veins: Implications for element transport, hydrogen production and life-supporting environment
603 formation. *Geochimica et Cosmochimica Acta* **141**, 454–471.
- 604 Plümper, O., Røyne, A., Magrasó, A. & Jamtveit, B. (2012). The interface-scale mechanism of reaction-induced
605 fracturing during serpentinization. *Geology* **40**, 1103–1106.
- 606 Putnis, A. (2002). Mineral replacement reactions: from macroscopic observations to microscopic mechanisms.
607 *Mineralogical Magazine* **66**, 689–708.
- 608 Ryu, K. W., Lee, M. G. & Jang, Y. N. (2011). Mechanism of tremolite carbonation. *Applied Geochemistry* **26**,
609 1215–1221.
- 610 Seyfried Jr, W. E. & Dibble Jr, W. E. (1980). Seawater-peridotite interaction at 300°C and 500 bars: implications
611 for the origin of oceanic serpentinites. *Geochimica et Cosmochimica Acta* **44**, 309–321.
- 612 Seyfried Jr., W. E., Foustoukos, D. I. & Fu, Q. (2007). Redox evolution and mass transfer during
613 serpentinization: An experimental and theoretical study at 200 °C, 500 bar with implications for
614 ultramafic-hosted hydrothermal systems at Mid-Ocean Ridges. *Geochimica et Cosmochimica Acta* **71**,
615 3872–3886.
- 616 Stawski, T. M., van Driessche, A. E., Ossorio, M., Rodriguez-Blanco, J. D., Besselink, R. & Benning, L. G.
617 (2016). Formation of calcium sulfate through the aggregation of sub-3 [thinsp] nanometre primary
618 species. *Nature communications* **7**.

- 619 Trittschack, R., Grobéty, B. & Brodard, P. (2013). Kinetics of the chrysotile and brucite dehydroxylation
620 reaction: a combined non-isothermal/isothermal thermogravimetric analysis and high-temperature X-
621 ray powder diffraction study. *Physics and Chemistry of Minerals* **41**, 197–214.
- 622 Trittschack, R., Grobéty, B. & Koch-Müller, M. (2012). In situ high-temperature Raman and FTIR spectroscopy
623 of the phase transformation of lizardite. *American Mineralogist* **97**, 1965–1976.
- 624 Turci, F., Tomatis, M., Lesci, I. G., Roveri, N. & Fubini, B. (2011). The Iron-Related Molecular Toxicity
625 Mechanism of Synthetic Asbestos Nanofibres: A Model Study for High-Aspect-Ratio Nanoparticles.
626 *Chemistry – A European Journal* **17**, 350–358.
- 627 Van Driessche, A., Benning, L., Rodriguez-Blanco, J., Ossorio, M., Bots, P. & García-Ruiz, J. (2012). The role
628 and implications of bassanite as a stable precursor phase to gypsum precipitation. *Science* **336**, 69–72.
- 629 Velbel, M. A. (1993). Formation of protective surface layers during silicate-mineral weathering under well-
630 leached, oxidizing conditions. *American Mineralogist* **78**, 405–405.
- 631 Velbel, M. A. (2009). Dissolution of olivine during natural weathering. *Geochimica et Cosmochimica Acta* **73**,
632 6098–6113.
- 633 Vils, F., Müntener, O., Kalt, A. & Ludwig, T. (2011). Implications of the serpentine phase transition on the
634 behaviour of beryllium and lithium-boron of subducted ultramafic rocks. *Geochimica et Cosmochimica*
635 *Acta* **75**, 1249–1271.
- 636 Viti, C. (2010). Serpentine minerals discrimination by thermal analysis. *American Mineralogist* **95**, 631–638.
- 637 Wang, J. A., Novaro, O., Bokhimi, X., Lopez, T., Gomez, R., Navarrete, J., Llanos, M. E. & Lopez-Salinas, E.
638 (1998). Characterizations of the thermal decomposition of brucite prepared by sol-gel technique for
639 synthesis of nanocrystalline MgO. *Materials Letters* **35**, 317–323.
- 640 Warren, B. E. (1969). *X-ray Diffraction*. Courier Corporation.
- 641 Whittaker, E. (1956a). The structure of chrysotile. II. Clino-chrysotile. *Acta Crystallographica* **9**, 855–862.
- 642 Whittaker, E. (1956b). The structure of chrysotile. III. Ortho-chrysotile. *Acta Crystallographica* **9**, 862–864.
- 643 Whittaker, E. (1956c). The structure of chrysotile. IV. Para-chrysotile. *Acta Crystallographica* **9**, 865–867.
- 644 Wicks, F. J. & O’Hanley, D. S. (1988). Serpentine minerals; structures and petrology. *Reviews in Mineralogy*
645 *and Geochemistry* **19**, 91–167.
- 646 Wicks, F. & Whittaker, E. (1977). Serpentine textures and serpentinization. *The Canadian Mineralogist* **15**, 459–
647 488.
- 648 Wunder, B. & Schreyer, W. (1997). Antigorite: High-pressure stability in the system MgO---SiO₂---H₂O
649 (MSH). *Lithos* **41**, 213–227.
- 650 Yada, K. (1967). Study of chrysotile asbestos by a high resolution electron microscope. *Acta Crystallographica*
651 **23**, 704–707.
- 652 Yada, K. & Iishi, K. (1974). Serpentine minerals hydrothermally synthesized and their microstructures. *Journal*
653 *of Crystal Growth* **24–25**, 627–630.
- 654 Yada, K. & Iishi, K. (1977). Growth and microstructure of synthetic chrysotile. *American Mineralogist* **62**, 958–
655 965.
- 656
- 657

658 **Table 1:** Summary of TGA weight loss data for samples series. Temperature ranges were
659 divided on the base of approximated TGA loss for molecular water (^α) brucite mineral (^γ) and
660 serpentine group minerals (^β).

661

662 **Table 2:** Summary of DTG and DTA peak temperatures for samples series corresponding to
663 curves on Fig. 2.

664

665 **Figure 1.** Thermal analyses of the sample series performed in N₂ atmosphere. 10 °C/min
666 heating rate and 0–800 °C temperature range. Thermogravimetric losses (TGA) are in wt%
667 and temperature deflection (DTA) are in °C. DTG has no unit. Typical dehydroxylation range
668 for brucite and serpentine dehydroxylation are also reported as well as typical serpentine
669 appearance (thick red arrow).

670

671 **Figure 2.** Representative samples powder TEM images for several reaction advancements. a)
672 flake-like particles (left and middle) and porous anastomosed medium with rare thick
673 individual tubular or conical fibers after 40 minutes, the Selected area (electron) diffraction is
674 around b) fibers like serpentine particles self-assembly (left and right) with individual brucite
675 (indicated by the white arrows) and aggregate (center) with few individual nanotubes after 1
676 hour, c) disoriented serpentine nanorods and individual poorly crystallized nanotubes after 1
677 hour and half (black arrows pin-pointed the beveled (conical) termination of serpentine
678 particles. The scale bar corresponds to 100 nm.

679

680 **Figure 3.** Representative samples powder TEM images of individual nanotubes after 2 hours
681 (a) and 2 hours 50 minutes (b) of reaction, typical width of chrysotile tunnel (8nm) and wall
682 (6 nm) is indicated in right-corner enlarged view, relicts of brucite is pin-pointed by the
683 arrow.

684

685 **Figure 4.** (a) Experimental structure factor patterns for different reaction advancements. Low
686 q region is enlarged in (b) (1.2-2 Å⁻¹ range), with the (004) diffraction peak indicated by the
687 white arrow. Brucite and the chrysotile end-member (3h of reaction) are reported as
688 references. (c) Pair Distribution Functions (PDFs) of experimental products at different
689 reaction times. The first 10 Å are enlarged in (d).

690

691 **Figure 5.** Experimental PDF patterns for different reaction advancement from Fig. 4c (solid
692 lines) and best fits from the linear combination (dotted lines) using brucite and chrysotile
693 (reference after 2h50 min of reaction) as the two mineral endmembers. The proportion of the
694 brucite component used for the simulations is also reported, for more detail refer to the text.

695

696 **Figure 6.** (a) Experimental structure pattern from Fig. 4b and (b) examples of modeled
697 structure factor patterns with the corresponding modelled structures (including one single
698 lizardite layers and multiple layers tubes) starting with a lizardite structure (inset).

699

700 **Figure 7.** Proposed conceptual model for chrysotile nucleation and growth mechanisms. From
701 left to right, structure evolution starts from single nano-sheets of serpentine, initial
702 dissolution-reprecipitation is accompanied by aggregation and stacking along c axis and size
703 homogeneization to form nanorods then monodisperse nanotubes assemblage.

704

705

	reaction time (min) this study						reaction time (min) Lafay et al., (2013)		
	40	60	90	120	145	170	360	720	1800
T range (°C)	TGA loss (%)						TGA loss (%)		
30-200^a	10.8	12.8	9.7	8.8	10.5	10.5	4.5	5.9	4
200-400^γ	10.3	9.7	7.6	3.4	2.6	2.2	2.7	1.8	1.1
400-800^β	8.5	6.9	8.2	10.5	13.6	11.5	12	11.1	12
sum at 800	29.6	29.4	25.5	22.7	26.7	24.2	19.2	18.8	17.1

Table1

Table 2

	reaction time (min)						Reaction time (min)		
	this study						Lafay et al., (2013)		
	40	60	90	120	145	170	360	720	1800
for DTG	277 w	344 ss	338 ss						
peak T°C	363 ss	391 sh	386 sh		460 ss	457 s	366 w		
	391 sh	625 w	537 s	553 ss	535 ss	554 ss	593 ss	600 ss	600 ss
	584 w								
	675 w								
for DTA	687 exo s	335 endo w	341 endo w	555 endo ss	457 endo s	552 endo s	599 endo w	590 endo w	594 endo w
peak T°C		634 exo s	541 endo w		536 endo s				
			687 exo ss	715 exo ss	670 exo ss	708 exo ss	775 exo ss	814 exo ss	827 exo ss

Note: w = weak, s = strong, ss = very strong (main peak), sh = shoulder, endo = endothermic, exo = exothermic

Figure 1

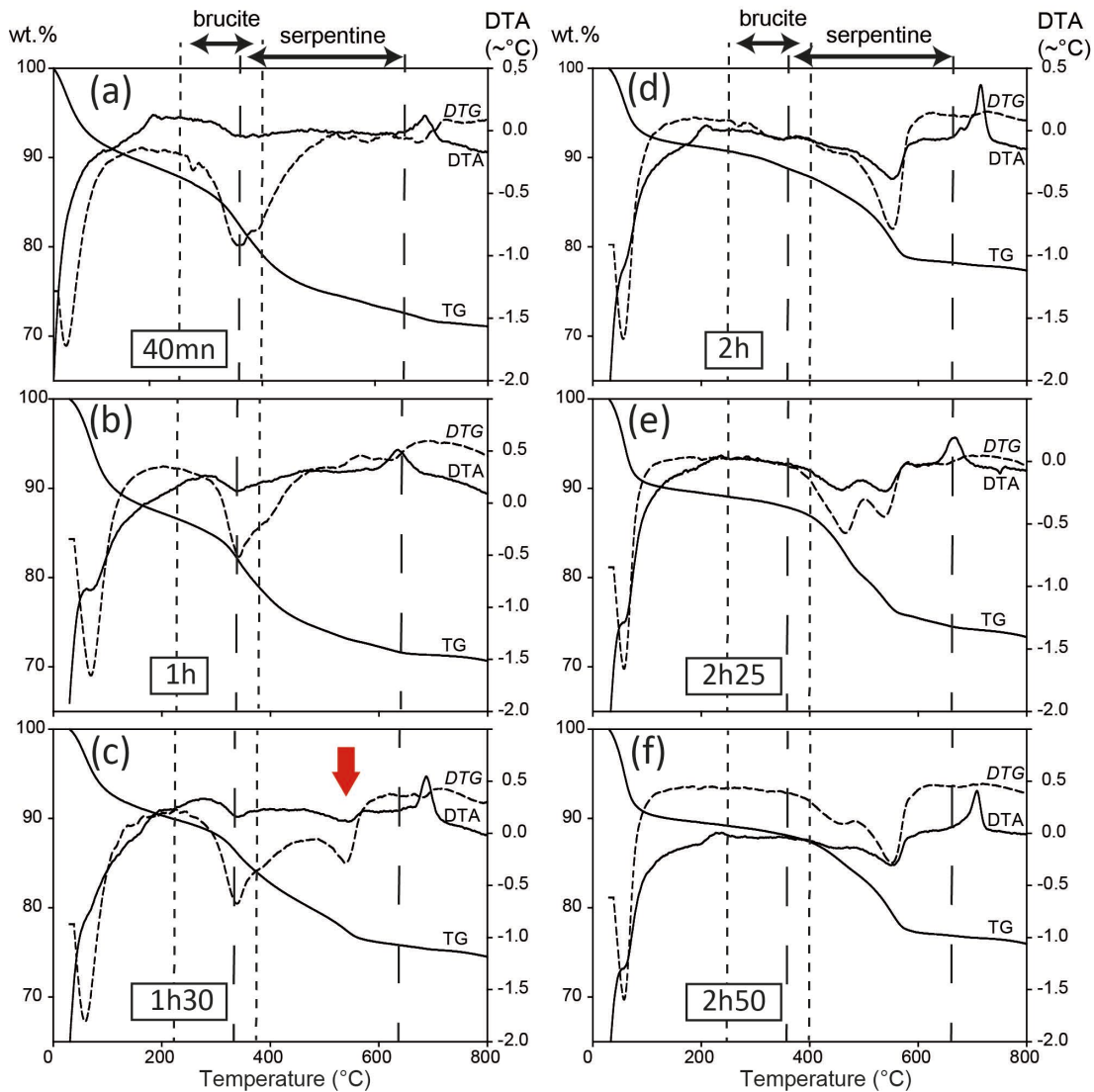


Figure 2

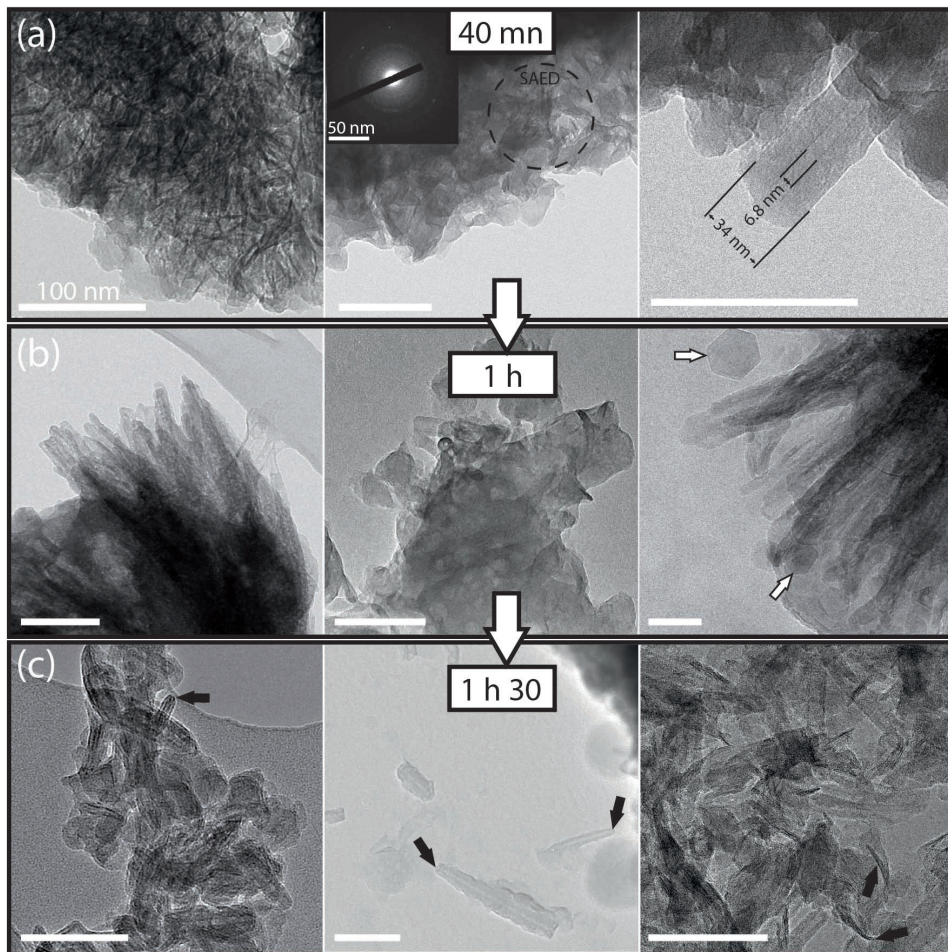


Figure 3

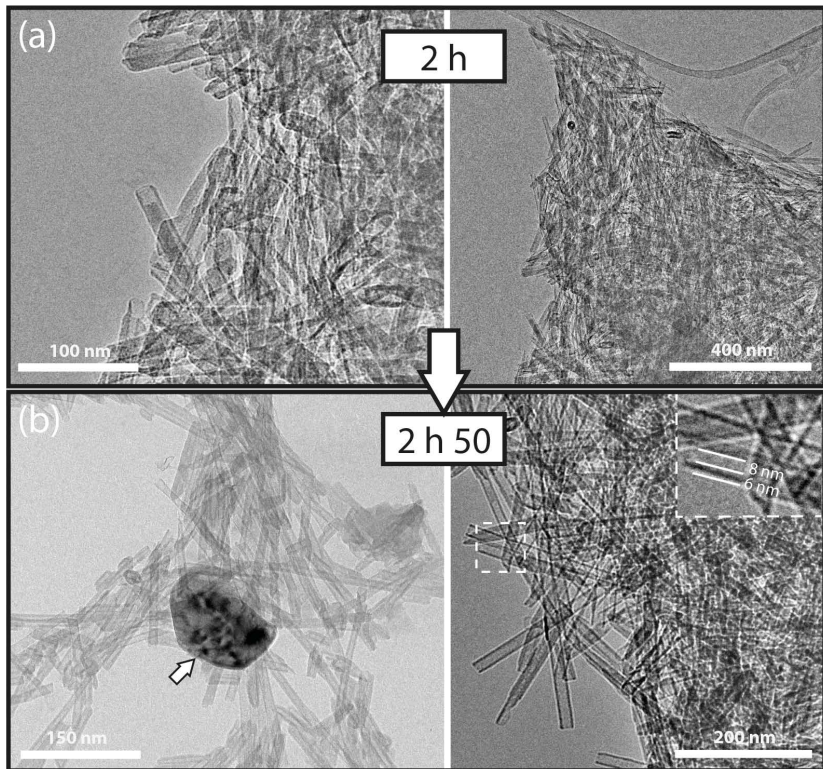


Figure 4

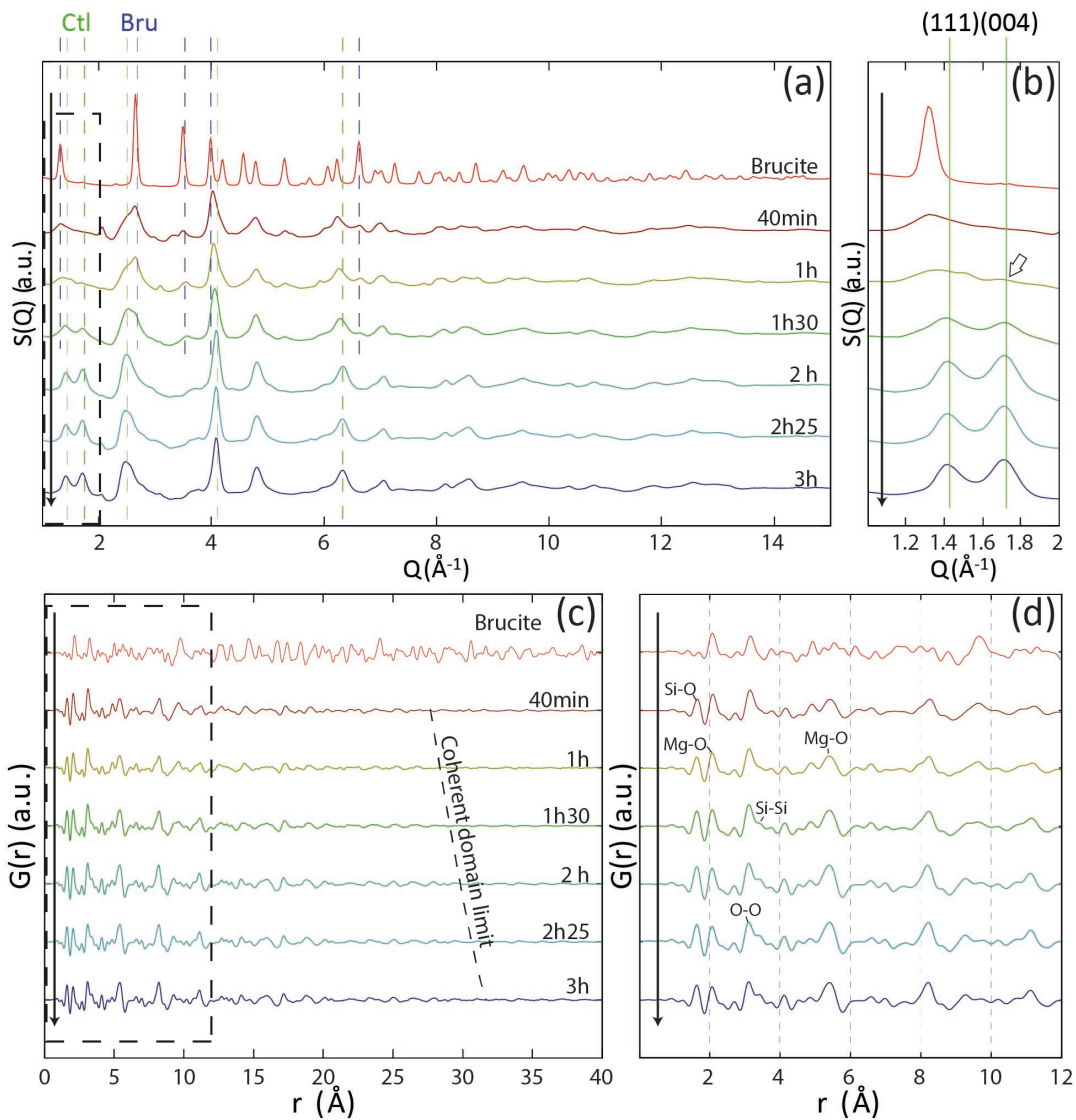


Figure 5

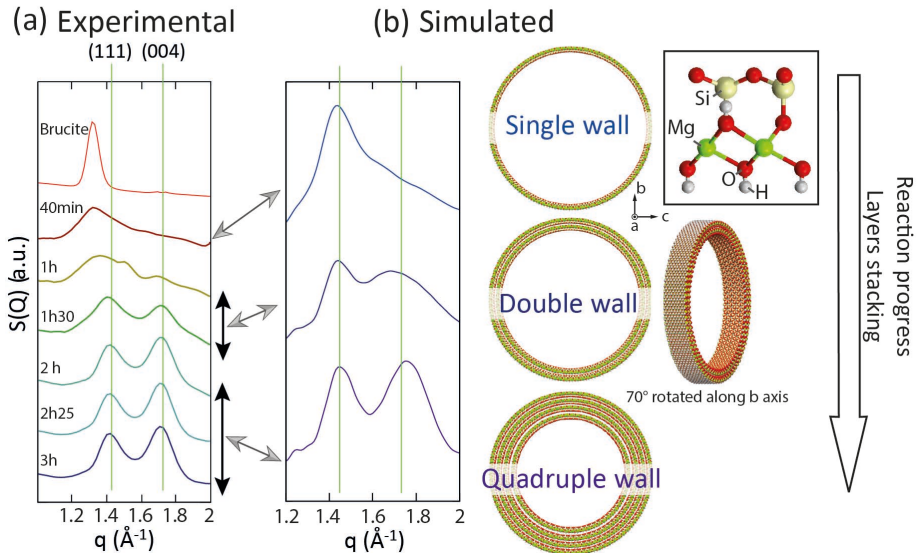


Figure 6

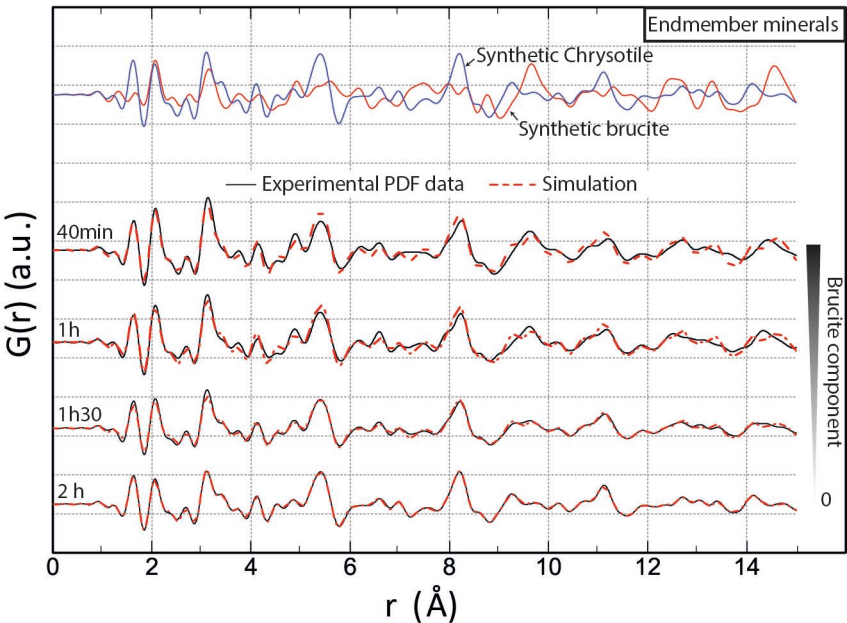


Figure 7

